ADVANCED MATERIALS INTERFACES
www.advmatinterfaces.de

Role of Stronger Interlayer van der Waals Coupling in Twin-Free Molecular Beam Epitaxy of 2D Chalcogenides

Wouter Mortelmans, Karel De Smet, Ruishen Meng, Michel Houssa, Stefan De Gendt, Marc Heyns, and Clement Merckling**

Large-area epitaxy of layered materials is one of the cornerstones for a successful exploitation of van der Waals (vdW) materials in the semiconductor industry. The formation of 60° twin stacking faults and 60° grain boundaries is of major concern for the defect-free epitaxial growth. Although strategies to overcome the occurrence of these defects are being considered, more fundamental understanding on the origin of these defects is highly essential. This work focuses on understanding the formation of 60° twins in (quasi-) vdW epitaxy of 2D chalcogenides. Molecular beam epitaxy (MBE) experiments reveal the striking difference in 60° twin occurrence between WSe_2 and Bi_2Se_3 in both quasi-vdW heteroepitaxy and vdW homoepitaxy. Density functional theory (DFT) calculations link this difference to the interlayer vdW coupling strength at the unit cell level. The stronger interlayer vdW coupling in Bi_2Se_3 unit cells compared to WSe_2 unit cells is explained to result in a reduced twin occurrence. Hence, such compounds show significantly more promise for defect-free epitaxial integration. This interesting aspect of (quasi-)vdW epitaxy reveals that the strength of interlayer vdW coupling is key for workable 2D materials and opens perspectives for other strongly coupled vdW materials.

1. Introduction

The discovery of graphene and its unique transport properties has boosted recent interests in a broad variety of 2D materials.[1,2] In this framework, layered chalcogenides are a promising class of 2D van der Waals (vdW) materials.[3–5] The transition metal dichalcogenides (TMDs) having the chemical form of MX_2 and the topological insulators (TIs) having the chemical form of group-V_2VI_3 are important examples. TMD materials such as WSe_2, MoS_2, etc. are highly interesting for opto- and nanoelectronics, thanks to their semiconducting properties and a direct bandgap at monolayer (ML) thickness.[6–11] TI materials such as Bi_2Se_3, Sb_2Te_3, etc. (and their alloys) are most promising for their strong spin–orbit coupling and band inversion, enabling new states of quantum matter useful for topological electronics.[12,13]

The large-area integration of 2D chalcogenides is of crucial importance for these materials to enable industry-compatible devices.[14] The growth of vdW materials through the process of epitaxy is one of the most promising approaches to meet the demanding requirements of single-crystalline quality, large-area uniformity, and large-scale throughput.[15] Therefore, the quasi-vdW and vdW epitaxy (2D-on-3D and 2D-on-2D, respectively) of layered chalcogenides is extensively being researched in the literature.[15–20] One of the major concerns in (quasi-) vdW epitaxy of these materials is the systematic formation of stacking faults like 60° twins, as observed in either molecular beam epitaxy (MBE) (quasi-vdW[21–29] and vdW[21,30–36]), metalorganic vapor phase epitaxy (quasi-vdW[21,37–42] and vdW[21,43,44]), and chemical vapor epitaxy (quasi-vdW[45–47] and vdW[48–53]). To mitigate the formation of these defects, several approaches are being reported that rely on optimized growth conditions,[54–56] buffer layer growth,[57] growth on h-BN templates,[54,58] or the introduction of a 3D aspect in the growth surface like surface roughness[59] or surface step edges.[60]

However, to date, a more fundamental understanding on the formation of 60° twin defects in (quasi-)vdW epitaxy of layered chalcogenides is highly required. A systematic comparative study focusing on the formation of twin defects is performed in this work for the epitaxy of various 2D chalcogenides using the MBE growth technique. The 2D chalcogenides that are studied are WSe_2 from the MX_2 family and Bi_2Se_3 from the group-V_2VI_3 family. The epitaxial processes include WSe_2 and Bi_2Se_3 quasi-vdW heteroepitaxy on on-axis *c*-plane sapphire substrates and

Dr. W. Mortelmans, Prof. M. Heyns, Dr. C. Merckling
KU Leuven
Department of Materials Engineering
Kasteelpark Arenberg 44, Leuven 3001, Belgium
E-mail: wmortel@mit.edu; clement.merckling@imec.be
Dr. W. Mortelmans, K. De Smet, Prof. M. Houssa, Prof. S. De Gendt, Prof. M. Heyns, Dr. C. Merckling
Imec
Kapeldreef 75, Leuven 3001, Belgium
K. De Smet, Prof. S. De Gendt
KU Leuven
Department of Chemistry
Celestijnenlaan 200f, Leuven 3001, Belgium
R. Meng, Prof. M. Houssa
KU Leuven
Department of Physics and Astronomy
Celestijnenlaan 200d, Leuven 3001, Belgium
The ORCID identification number(s) for the author(s) of this article can be found under https://doi.org/10.1002/admi.202100438.

DOI: 10.1002/admi.202100438

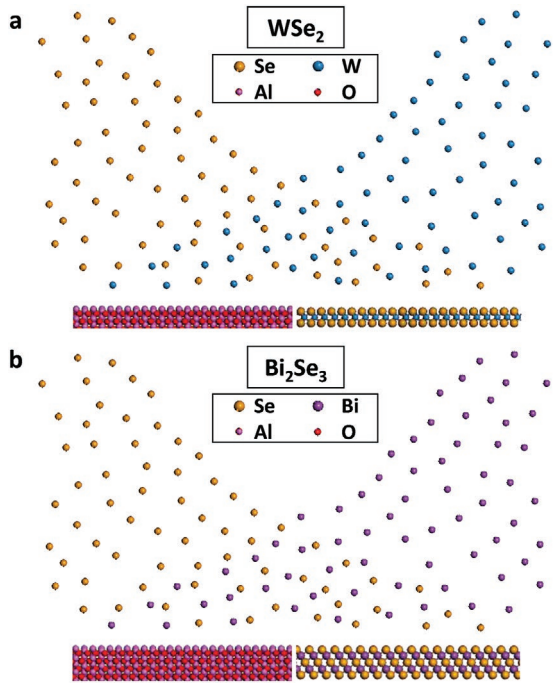

Figure 1. Simplified schematic illustration of the experimental setup used to study the MBE (quasi-)vdW epitaxy of WSe_2 and Bi_2Se_3 on sapphire and on respectively WSe_2 and Bi_2Se_3 surfaces. a) WSe_2 PA-MBE method relying on the electron-beam evaporation of elemental W and H_2Se plasma. b) Bi_2Se_3 PA-MBE method relying on the thermal evaporation of elemental Bi and H_2Se plasma.

WSe_2 and Bi_2Se_3 vdW homoepitaxy on respectively WSe_2(0001) and Bi_2Se_3(0001) exfoliated flakes. The similarities and differences of the various epitaxy processes are discussed and density functional theory (DFT) calculations are performed to shine more light on the fundamental aspect of 60° twin formation.

2. Experimental Section

The experimental methodology that is applied for the 2D chalcogenide MBE processes is illustrated using simplified schematics in **Figure 1**. The (1 × 1) reconstructed sapphire surfaces were obtained by thermal annealing at ≈900 °C under H_2 as reported and characterized previously.[23] The virtual WSe_2(0001) and Bi_2Se_3(0001) substrates were fabricated relying on mechanical exfoliation on silicon substrates.[33,34] The epitaxies were performed using plasma-assisted (PA-)MBE with H_2X radio frequency (RF) plasma sources[61] and electron-beam evaporation of elemental W transition metals (Figure 1a) and thermal evaporation of elemental Bi metals (Figure 1b). For the WSe_2 compound, the growths occurred at a temperature of 450 °C with low growth rates of ≈0.1–1.3 ML h^{-1}, driven by the W evaporation flux. The growths of the Bi_2Se_3 compound occurred at a lower temperature of 160 °C with higher growth rates of ≈5–12 ML h^{-1}, and similarly, driven by the Bi evaporation flux. In both cases, the higher growth rates corresponded to the quasi-vdW heteroepitaxies and the lower growth rates to the vdW homoepitaxies. The H_2Se fluxes were set to a total and maximal pressure of ≈2.0×10^{-5} Torr in the RF plasma source. More details on these conditions and their justification are found in the Supporting Information.

3. Results and Discussion

3.1. Quasi-vdW Heteroepitaxy

The quasi-vdW heteroepitaxies of WSe_2 and Bi_2Se_3 on the sapphire surfaces are presented in **Figure 2**. They represent 1 ML of WSe_2 (Figure 2a,b) and 1 ML of Bi_2Se_3 (Figure 2c,d) on (1 × 1) *c*-plane sapphire substrates. The single-layer thickness is chosen to maximize the amount of quasi-vdW heteroepitaxy while avoiding the vdW homoepitaxy of the 2nd ML on the 1st ML. The atomic force microscopy (AFM) data of the sapphire substrate and the quasi-vdW heteroepitaxies are discussed in the Supporting Information.

The polar reflection high-energy electron diffraction (RHEED) characterization of the WSe_2 quasi-vdW heteroepitaxy clearly reveals the in-plane epitaxial registry of the WSe_2 crystals with the underlying Al_2O_3 surface (Figure 2a). The epitaxial relation is highlighted using yellow and blue diamonds for respectively WSe_2 and Al_2O_3 and is characterized as $[11\bar{2}0]$

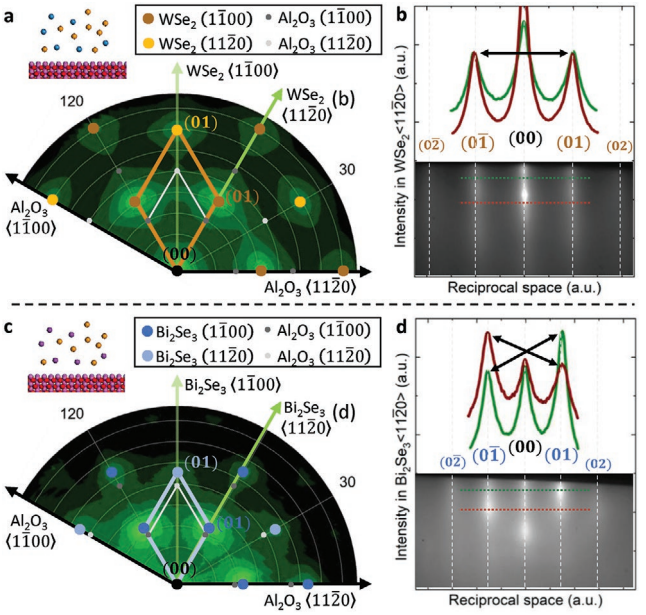

Figure 2. Epitaxial registry and preferred stacking in MBE quasi-vdW heteroepitaxy of 2D chalcogenides. a,b) The top panel corresponds to the WSe_2 quasi-vdW heteroepitaxy on (1 × 1) sapphire. c,d) The bottom panel corresponds to the Bi_2Se_3 quasi-vdW heteroepitaxy on (1 × 1) sapphire. (a,c) Azimuthal RHEED scans overlaid with yellow (WSe_2) and purple (Bi_2Se_3) dots representing the diffractions of respectively WSe_2 and Bi_2Se_3 and with blue dots representing the ones of α-Al_2O_3. The diamond reveals the in-plane alignment of the grown vdW crystals with respect to the Al_2O_3 surface underneath. (b,d) RHEED intensity line profiles and pattern in respectively the WSe_2 $\langle 11\bar{2}0 \rangle$ and the Bi_2Se_3 $\langle 11\bar{2}0 \rangle$ direction. The equivalent $(0\bar{1})$ and (01) diffraction streaks of the WSe_2 and the inequivalent $(0\bar{1})$ and (01) diffraction streaks of the Bi_2Se_3 demonstrate respectively the absence and presence of the threefold in-plane characteristic hence the preferred threefold symmetric stacking in the quasi-vdW heteroepitaxy on sapphire.

$WSe_2(0001)//[11\bar{2}0]\,Al_2O_3(0001)$. This is a similar epitaxial relationship as previously reported for the growths of WSe_2/MoS_2 on various reconstructed sapphire surfaces.[21,23,37] The identical $(0\bar{1})$ and (01) diffraction streaks observed from the diffraction patterns uncover an important limitation of the quasi-vdW epitaxy experiment. In Figure 2b, the RHEED pattern in the WSe_2 $\langle 11\bar{2}0\rangle$ direction is presented where several intensity line profiles are extracted from various "k_z" positions that give information about the out-of-plane ordering of the grown 2D crystal planes.[62] The equivalent intensities of the $(0\bar{1})$ and (01) diffraction streaks confirm the absence of the expected threefold symmetric stacking hence the abundant presence of 60° twins.[26] This results from the lack of a preferred stacking in the $[11\bar{2}0]\,WSe_2(0001)//[11\bar{2}0]\,Al_2O_3(0001)$ registry and consequently results in a high defect density of 60° grain boundaries which is known from literature to impact device performances.[63,64]

A striking difference with respect to WSe_2 quasi-vdW heteroepitaxy is observed in Bi_2Se_3 quasi-vdW heteroepitaxy. This is obtained from the polar RHEED characterization presented in Figure 2c,d. The epitaxial relation of the Bi_2Se_3 with the (1×1) sapphire surface is similar as for the case of WSe_2: $[11\bar{2}0]\,Bi_2Se_3(0001)//[11\bar{2}0]\,Al_2O_3(0001)$ (Figure 2c, purple and blue diamonds for respectively Bi_2Se_3 and Al_2O_3). However, the stacking preference and hence the occurrence of 60° twins (and 60° grain boundaries) is dissimilar. This is corroborated from the inequivalent $(0\bar{1})$ and (01) diffraction streaks of the Bi_2Se_3 quasi-vdW heteroepitaxy as observed from the Bi_2Se_3 $\langle 11\bar{2}0\rangle$ RHEED pattern (Figure 2d). The observation of these inequivalent streaks is in agreement with the threefold in-plane rotational symmetry of the Bi_2Se_3 crystal structure, and confirms the preferred and unique stacking of Bi_2Se_3 on sapphire and hence the reduced formation of 60° twins.[65] In summary, Bi_2Se_3 quasi-vdW heteroepitaxy on sapphire is less prone to stacking fault formation compared to WSe_2 (and in general TMDs[21,34]), despite the equivalent in-plane crystal structure symmetry and presence of vdW gap in both compounds. Consequently, Bi_2Se_3 shows significantly more promise for defect-free epitaxial integration.

3.2. VdW Homoepitaxy

To further explore these interesting differences, a study is presented based on vdW homoepitaxy of the highlighted 2D chalcogenides. The vdW homoepitaxy experiments represent ≈1/3 ML of WSe_2 and Bi_2Se_3 grown on respectively exfoliated $WSe_2(0001)$ and $Bi_2Se_3(0001)$ flakes, obtained by a reduction of the growth rate compared to the experiments performed on sapphire. Such partial ML thickness is preferred here, to enable the identification of the individual grown 2D chalcogenide crystals before coalescence and to avoid the onset of multilayer growth. The limited lateral sizes of the exfoliated flakes make RHEED characterization impractical. The focus is therefore set to AFM analysis.

The WSe_2 vdW homoepitaxy is identified by a high density of characteristic triangular grains with crystal sizes up to ≈50 nm. This is observed from the AFM image presented in **Figure 3**a. The algorithmic analysis[33] of the WSe_2 crystals nucleated and grown on the $WSe_2(0001)$ surface enables to qualify the epitaxial relation and to reveal the presence of a preferred stacking. The

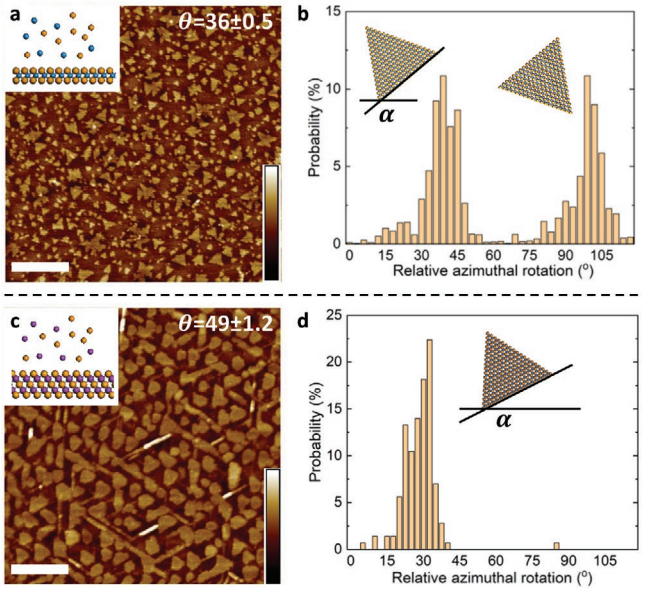

Figure 3. Epitaxial registry and preferred stacking in MBE vdW homoepitaxy of 2D chalcogenides. a,b)The top panel corresponds to the WSe_2 vdW homoepitaxy on $WSe_2(0001)$ surfaces. c,d) The bottom panel corresponds to the Bi_2Se_3 vdW homoepitaxy on $Bi_2Se_3(0001)$ surfaces. (a,c) AFM images of respectively the WSe_2 and Bi_2Se_3 vdW homoepitaxy. θ corresponds to surface coverage in %. Scale bars are 200 nm. Height scales are 2 and 3 nm in (a,c) respectively. (b,d) Analyses of the AFM images in (a,c) highlighting the relative azimuthal in-plane distribution of the nucleation and grown crystals in respectively the WSe_2 and Bi_2Se_3 vdW homoepitaxy. The sixfold periodicity of the WSe_2 crystals and the threefold periodicity of the Bi_2Se_3 crystals demonstrate respectively the absence and presence of a preferred stacking in the vdW homoepitaxial registry.

distribution of the relative azimuthal in-plane orientation of the analyzed WSe_2 triangular grains is presented in Figure 3b. This distribution with a 60° difference between both consecutive peaks clearly reveals the sixfold in-plane periodicity, which is reported to result from the inability to control the bilayer stacking phase.[33] Consequently, both the 2H and 3R stacking phases are simultaneously present in the vdW homoepitaxy resulting in the presence of a high density of 60° twins and 60° grain boundaries upon closure of the ML. Hence, our AFM and RHEED studies have shown that in both vdW homoepitaxy and quasi-vdW heteroepitaxy, the WSe_2 compound systematically yields severe formation of stacking faults which is emphasized to be very challenging to control.

This observation is once more significantly different in the Bi_2Se_3 growth. The AFM characterization and crystal analysis of the Bi_2Se_3 vdW homoepitaxy is presented in Figure 3c,d. The Bi_2Se_3 vdW homoepitaxy yields characteristic equilateral triangles having a crystal grain size up to ≈100 nm, and a threefold periodic in-plane alignment of the nucleated and grown crystals as in agreement with the symmetry of the Bi_2Se_3 crystal structure. The larger grain size is linked with the larger vapor pressure of the elemental bismuth, since adatom diffusion is previously reported to correlate with vapor pressure in vdW epitaxy of TMDs by MBE.[34,66] The Bi_2Se_3 vdW compound does not suffer from the fundamental limitation of stacking fault formation in vdW homoepitaxy as generally observed in TMD vdW compounds.[21,33,34] This opens a window for defect-free integration

of Bi_2Se_3 through the growth process of vdW homoepitaxy, and possibly also for other related vdW compounds.

3.3. Density Functional Theory

Theoretical DFT calculations are presented for the highlighted 2D chalcogenide materials, WSe_2 and Bi_2Se_3, to understand the striking differences in twin defect formation that are observed from the experimental data. The focus is placed on DFT calculations for the homoepitaxy cases. A generalization of these outcomes could be extended to the heteroepitaxy cases. The calculated binding energies using periodic structures are reasonable estimates of the binding energy of nuclei that consist of numerous unit cells.

In **Figure 4**, the binding energies of WSe_2 and Bi_2Se_3 are calculated for the set of most stable bilayer stacking configurations (details in the Supporting Information). The numerical values of the calculated binding energies are expressed in meV per unit cell (uc) and are presented in Figure 4a, with left and right axes corresponding to respectively WSe_2 and Bi_2Se_3. The various unit cell stacking configurations are defined by considering a bilayer representation of the atomic layers at the interface, as schematically illustrated in Figure 4b. The unit cell stacking configurations are then noted by assigning a letter for each bilayer at the interface in agreement with the void spaces A, B, and C, and a prime (′) is used when the bonding symmetry of the top bilayer is inversed with respect to the bonding symmetry of the bottom bilayer (see Figure 4b). This notation and bilayer representation enables an appropriate and physically relevant comparison between WSe_2 and Bi_2Se_3 units that respectively have a triple- and quintuple-layer structure.

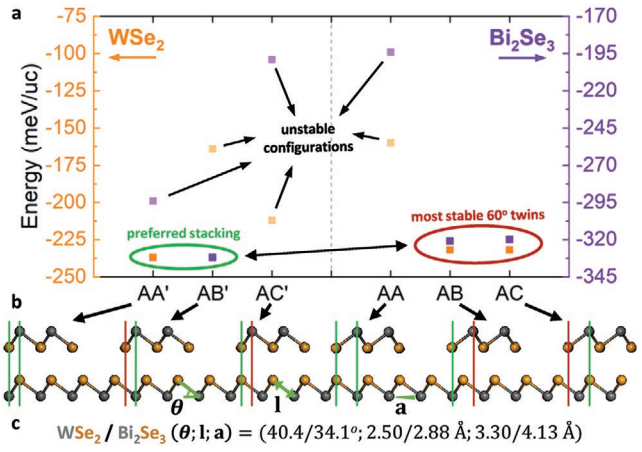

Figure 4. Binding energy from DFT calculations for 2D chalcogenides. a) Calculated binding energy in meV per unit cell for both WSe_2 and Bi_2Se_3 bilayer homostructures in function of the bilayer stacking configuration. The WSe_2 binding energies are plotted on the left *Y*-axis (yellow). The Bi_2Se_3 binding energies—that are significantly larger—are plotted on the right *Y*-axis (purple). b) Definition, schematic illustration, and notation of the various stacking configurations based on a bilayer representation of the atomic layers at the interface. Gray corresponds to the metal atom and yellow to the chalcogen atom. c) Numerical values of the bond angle, bond length, and lattice parameter for both WSe_2 and Bi_2Se_3 for the representation used in (b).

The usage of the prime (′) easily separates the 0° from the 60° twin, and results in six possible unit cell stacking configurations for each vdW compound (AA″, AB″, AC′, AA, AB, and AC). In Figure 4c, the bond angle (θ), bond length (l), and lattice parameter (a) of both compounds are given to justify the representation used in Figure 4b.

The DFT calculations reveal two important aspects. The first aspect concerns the comparison of the most preferred stacking with the most preferred 60° twin for each vdW compound. As seen from Figure 4a, the preferred unit cell stacking in WSe_2 is noted as AA′ and has two stable 60° twins noted as AB and AC. The comparison of these configurations reveals that 60° twins in WSe_2 (AB and AC) are slightly less stable having a binding energy difference of ≈6 meV per uc (≈2.4%) compared to the most preferred unit cell stacking (AA′). In the case of Bi_2Se_3, the most perfect unit cell stacking is noted as AB′ and similarly has two stable 60° twins (AB and AC). The preference of AB′ for Bi_2Se_3 compared to AA′ for WSe_2 could be linked to the differences in the unit cells like bond angle, bond length and lattice parameter (Figure 4c). The comparison reveals that for Bi_2Se_3, 60° twins are ≈11 meV per uc (≈3.4%) less stable compared to the preferred unit cell stacking. Hence, both WSe_2 and Bi_2Se_3 only have very subtle differences in unit cell binding energy between 0° and 60° twins, and it is unlikely that the slightly larger imbalance in Bi_2Se_3 is fully responsible for the experimentally observed striking difference in 60° twin defect formation.

The second important aspect that is revealed from our DFT calculations is related to the absolute unit cell binding energies of the two vdW compounds. From Figure 4a, it is obvious that the binding energy in the Bi_2Se_3 unit cell, in general, is larger compared to the binding energy in the WSe_2 unit cell.[67] This can be seen from the absolute values and energy-range difference of the WSe_2 and Bi_2Se_3 axes (left and right, respectively) in Figure 4a. In the preferred stacking, the Bi_2Se_3 unit cell results in an ≈94 meV per uc (≈40%) lower (i.e., stronger binding) energy compared to the WSe_2 unit cell. It is this substantially stronger vdW interlayer coupling in Bi_2Se_3 unit cells that could explain the striking difference in twin defect formation.

The statement made above is supported by DFT calculations that consider the alteration of the unit cell stacking configuration by nucleus rotation. In **Figure 5**, the energy per unit cell (relative to the most preferred stacking) for the stacking alteration from the most preferred stacking configuration to the most preferred 60° twin is presented. In the case of WSe_2 unit cells (left panel), this is respectively from AA′ to AB. In the case of Bi_2Se_3 unit cells (right panel), this is respectively from AB′ to AB. As a result of the stronger interlayer vdW coupling in Bi_2Se_3 unit cells, the energy barrier for unit cell stacking alteration by nucleus rotation is significantly higher ($E_{barrier}$ = 122.2 meV per uc for Bi_2Se_3, compared to $E_{barrier}$ = 44.1 meV per uc for WSe_2). This is consequently related to the larger amount of energy that is required to rotate the Bi_2Se_3 nucleus from its stronger epitaxial registry with the underlying surface, and could be a potential mechanism obstructing the severe formation of 60° twins.

Moreover, the thermal energy per unit cell to enable this nucleus rotation from 0° to 60° is found insufficient to overcome this energy barrier ($E_{barrier}$) for the case of Bi_2Se_3 homoepitaxy ($E_{thermal}$ = 39.5 meV per uc at T_g = 160 °C), while it is found

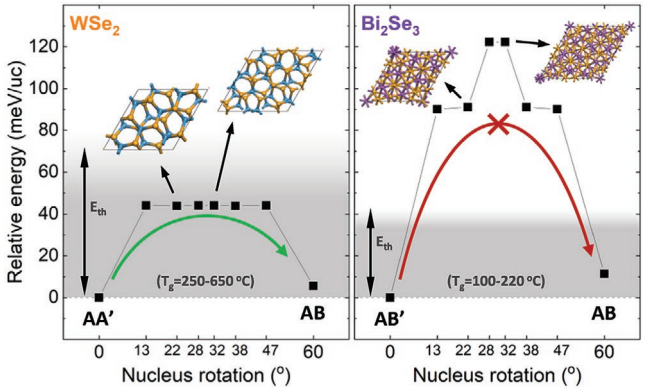

Figure 5. Stacking alteration by nucleus rotation from DFT calculations for 2D chalcogenides. Representation of the relative energy in meV per unit cell (left panel WSe_2, right panel Bi_2Se_3) for stacking alteration from the most preferred stacking configuration to the next stable 60° twin. Top-view ball-and-stick schematic illustrations of the intermediated structures at rotation angles of 22° and 32° are illustrated on top of the figure. The thermal energy available per unit cell is shaded in gray for both WSe_2 (T_g = 450 °C) and Bi_2Se_3 (T_g = 160 °C) epitaxy.

sufficient for the case of WSe_2 homoepitaxy ($E_{thermal}$ = 64.5 meV per uc at T_g = 450 °C) (see Figure 5 gray zone). This would result in a more challenging and hampered Bi_2Se_3 nuclei rotation during nucleation/growth compared to WSe_2 nuclei, and could confirm the remarkable enhanced control on 60° twin defect formation in Bi_2Se_3 homoepitaxy and its related epitaxy processes.

4. Conclusion

It is shown how the formation of 60° twin defects in Bi_2Se_3 epitaxy is fundamentally better controlled compared to WSe_2 epitaxy. The quasi-vdW heteroepitaxy and vdW homoepitaxy of WSe_2 systematically yield a high density of stacking faults resulting from 1) the calculated subtle differences in unit cell binding energy for the 0° and 60° configurations and 2) the weak vdW interlayer coupling in the WSe_2 units. In Bi_2Se_3, the threefold character of the quasi-vdW heteroepitaxy and vdW homoepitaxy clearly reveal the striking difference having a preferred stacking sequence and reduced presence of 60° twin defects. Despite the similar subtle differences in unit cell binding energy for the 0° and 60° configurations, this is explained by the stronger interlayer vdW coupling in the Bi_2Se_3 unit cells.

Stronger interlayer vdW coupling challenges nucleus rotation from the most stable 0° configuration to the next stable 60° twin. The formation of 60° twins in (quasi-)vdW epitaxy is therefore not only related to the difference in unit cell binding energy between the 0° and 60° configurations, but also to the absolute strengths of the interlayer vdW interactions between the unit cells. The strength of the interlayer unit cell coupling becomes hence a crucial parameter to control the defect-density of epitaxially grown 2D chalcogenides. This opens perspectives for Bi_2Se_3 and other related vdW compounds with strong interlayer unit cell coupling to further accelerate the defect-free epitaxial growth of 2D materials. With the insights generated in this study on 60° twin formation in (quasi-)vdW epitaxy, a first step is taken for the development of mitigation strategies emphasizing on the control of the interlayer interaction strength.

Supporting Information

Supporting Information is available from the Wiley Online Library or from the author.

Acknowledgements

The authors acknowledge the Horizon 2020 FETPROAC project SKYTOP – 824123 - "Skyrmion – Topological Insulator and Weyl Semimetal Technology". Part of the computational resources and services used in this work were provided by the VSC (Flemish Supercomputer Center), funded by the Research Foundation Flanders (FWO) and the Flemish Government, department EWI.

Conflict of Interest

The authors declare no conflict of interest.

Data Availability Statement

The data that support the findings of this study are available from the corresponding author upon reasonable request.

Keywords

2D chalcogenides, density functional theory, molecular beam epitaxy, stacking faults, van der Waals epitaxy

Received: March 17, 2021
Revised: April 17, 2021
Published online:

[1] K. S. Novoselov, A. K. Geim, S. V. Morozov, D. Jiang, Y. Zhang, S. V. Dubonos, I. V. Grigorieva, A. A. Firsov, *Science* **2004**, *306*, 666.
[2] A. K. Geim, I. V. Grigorieva, *Nature* **2013**, *499*, 419.
[3] D. Akinwande, C. Huyghebaert, C. H. Wang, M. I. Serna, S. Goossens, L. J. Li, H. S. P. Wong, F. H. L. Koppens, *Nature* **2019**, *573*, 507.
[4] Y. Liu, N. O. Weiss, X. Duan, H. C. Cheng, Y. Huang, X. Duan, *Nat. Rev. Mater.* **2016**, *1*, 16042.
[5] J. A. Robinson, *APL Mater.* **2018**, *6*, 058202.
[6] K. Kang, S. Xie, L. Huang, Y. Han, P. Y. Huang, K. F. Mak, C. J. Kim, D. Muller, J. Park, *Nature* **2015**, *520*, 656.
[7] J. R. Schaibley, H. Yu, G. Clark, P. Rivera, J. S. Ross, K. L. Seyler, W. Yao, X. Xu, *Nat. Rev. Mater.* **2016**, *1*, 16055.
[8] V. Sorkin, H. Pan, H. Shi, S. Y. Quek, Y. W. Zhang, *Crit. Rev. Solid State Mater. Sci.* **2014**, *39*, 319.
[9] Y. Zhang, T. R. Chang, B. Zhou, Y. T. Cui, H. Yan, Z. Liu, F. Schmitt, J. Lee, R. Moore, Y. Chen, H. Lin, H. T. Jeng, S. K. Mo, Z. Hussain, A. Bansil, Z. X. Shen, *Nat. Nanotechnol.* **2014**, *9*, 111.
[10] B. Radisavljevic, A. Radenovic, J. Brivio, V. Giacometti, A. Kis, *Nat. Nanotechnol.* **2011**, *6*, 147.

[11] Q. H. Wang, K. Kalantar-Zadeh, A. Kis, J. N. Coleman, M. S. Strano, *Nat. Nanotechnol.* **2012**, *7*, 699.
[12] J. E. Moore, *Nature* **2010**, *464*, 194.
[13] P. Liu, J. R. Williams, J. J. Cha, *Nat. Rev. Mater.* **2019**, *4*, 479.
[14] C. Huyghebaert, T. Schram, Q. Smets, T. Kumar Agarwal, D. Verreck, S. Brems, A. Phommahaxay, D. Chiappe, S. El Kazzi, C. Lockhart De La Rosa, G. Arutchelvan, D. Cott, J. Ludwig, A. Gaur, S. Sutar, A. Leonhardt, D. Marinov, D. Lin, M. Caymax, I. Asselberghs, G. Pourtois, I. P. Radu, *Technical Digest on Int. Electron Devices Meeting (IEDM)*, IEEE, MD, USA **2018**, p. 22.1.1.
[15] W. Mortelmans, S. De Gendt, M. Heyns, C. Merckling, *Appl. Mater. Today* **2021**, *22*, 100975.
[16] T. Tian, C. J. Shih, *Ind. Eng. Chem. Res.* **2017**, *56*, 10552.
[17] U. W. Pohl, *Epitaxy of Semiconductors Introduction to Physical Principles*, Springer, Berlin **2013**.
[18] L. A. Walsh, C. L. Hinkle, *Appl. Mater. Today* **2017**, *9*, 504.
[19] A. Koma, *J. Cryst. Growth* **1999**, *201*, 236.
[20] F. S. Ohuchi, B. A. Parkinson, K. Ueno, A. V. D. Koma, *J. Appl. Phys.* **1990**, *68*, 2168.
[21] W. Mortelmans, S. El Kazzi, B. Groven, A. Nalin Mehta, Y. Balaji, S. De Gendt, M. Heyns, C. Merckling, *Appl. Phys. Lett.* **2020**, *117*, 033101.
[22] S. Vishwanath, X. Liu, S. Rouvimov, P. C. Mende, A. Azcatl, S. McDonnell, R. M. Wallace, R. M. Feenstra, J. K. Furdyna, D. Jena, H. G. Xing, *2D Mater.* **2015**, *2*, 024007.
[23] W. Mortelmans, S. El Kazzi, A. Nalin Mehta, D. Vanhaeren, T. Conard, J. Meersschaut, T. Nuytten, S. De Gendt, M. Heyns, C. Merckling, *Nanotechnology* **2019**, *30*, 465601.
[24] C. H. Lee, S. Krishnamoorthy, D. J. O'Hara, M. R. Brenner, J. M. Johnson, J. S. Jamison, R. C. Myers, R. K. Kawakami, J. Hwang, S. Rajan, *J. Appl. Phys.* **2017**, *121*, 094302.
[25] M. W. Chen, H. K. Kim, D. Ovchinnikov, A. Kuc, T. Heine, O. Renault, A. Kis, *npj 2D Mater. Appl.* **2018**, *2*, 2.
[26] A. Ohtake, Y. Sakuma, *J. Phys. Chem. C* **2020**, *124*, 5196.
[27] X. Guo, Z. J. Xu, H. C. Liu, B. Zhao, X. Q. Dai, H. T. He, J. N. Wang, H. J. Liu, W. K. Ho, M. H. Xie, *Appl. Phys. Lett.* **2013**, *102*, 151604.
[28] J. E. Boschker, J. Momand, V. Bragaglia, R. Wang, K. Perumal, A. Giussani, B. J. Kooi, H. Riechert, R. Calarco, *Nano Lett.* **2014**, *14*, 3534.
[29] D. Kriegner, P. Harcuba, J. Veselý, A. Lesnik, G. Bauer, G. Springholz, V. Holý, *J. Appl. Crystallogr.* **2017**, *50*, 369.
[30] Y. Ma, S. Kolekar, H. Coy Diaz, J. Aprojanz, I. Miccoli, C. Tegenkamp, M. Batzill, *ACS Nano* **2017**, *11*, 5130.
[31] R. Yue, Y. Nie, L. A. Walsh, R. Addou, C. Liang, N. Lu, A. T. Barton, H. Zhu, Z. Che, D. Barrera, L. Cheng, P. R. Cha, Y. J. Chabal, J. W. P. Hsu, J. Kim, M. J. Kim, L. Colombo, R. M. Wallace, K. Cho, C. L. Hinkle, *2D Mater.* **2017**, *4*, 045019.
[32] J. Hall, B. Pielić, C. Murray, W. Jolie, T. Wekking, C. Busse, M. Kralj, T. Michely, *2D Mater.* **2018**, *5*, 025005.
[33] W. Mortelmans, A. Nalin Mehta, Y. Balaji, S. El Kazzi, S. Sergeant, M. Houssa, S. De Gendt, M. Heyns, C. Merckling, *2D Mater.* **2020**, *7*, 025027.
[34] W. Mortelmans, A. Nalin Mehta, Y. Balaji, S. Sergeant, R. Meng, M. Houssa, S. De Gendt, M. Heyns, C. Merckling, *ACS Appl. Mater. Interfaces* **2020**, *12*, 27508.
[35] C. Vergnaud, M. T. Dau, B. Grévin, C. Licitra, A. Marty, H. Okuno, M. Jamet, *Nanotechnology* **2020**, *31*, 255602.
[36] K. H. M. Chen, H. Y. Lin, S. R. Yang, C. K. Cheng, X. Q. Zhang, C. M. Cheng, S. F. Lee, C. H. Hsu, Y. H. Lee, M. Hong, J. Kwo, *Appl. Phys. Lett.* **2017**, *111*, 083106.
[37] J. Mo, S. El Kazzi, W. Mortelmans, A. N. Mehta, S. Sergeant, Q. Smets, I. Asselberghs, C. Huyghebaert, *Nanotechnology* **2020**, *31*, 125604.
[38] Y. C. Lin, B. Jariwala, B. M. Bersch, K. Xu, Y. Nie, B. Wang, S. M. Eichfeld, X. Zhang, T. H. Choudhury, Y. Pan, R. Addou, C. M. Smyth, J. Li, K. Zhang, M. A. Haque, S. Fölsch, R. M. Feenstra, R. M. Wallace, K. Cho, S. K. Fullerton-Shirey, J. M. Redwing, J. A. Robinson, *ACS Nano* **2018**, *12*, 965.
[39] X. Zhang, T. H. Choudhury, M. Chubarov, Y. Xiang, B. Jariwala, F. Zhang, N. Alem, G. C. Wang, J. A. Robinson, J. M. Redwing, *Nano Lett.* **2018**, *18*, 1049.
[40] S. M. Eichfeld, V. O. Colon, Y. Nie, K. Cho, J. A. Robinson, *2D Mater.* **2016**, *3*, 025015.
[41] D. Chiappe, J. Ludwig, A. Leonhardt, S. El Kazzi, A. Nalin Mehta, T. Nuytten, U. Celano, S. Sutar, G. Pourtois, M. Caymax, K. Paredis, W. Vandervorst, D. Lin, S. De Gendt, K. Barla, C. Huyghebaert, I. Asselberghs, I. Radu, *Nanotechnology* **2018**, *29*, 425602.
[42] M. Marx, A. Grundmann, Y. R. Lin, D. Andrzejewski, T. Kümmell, G. Bacher, M. Heuken, H. Kalisch, A. Vescan, *J. Electron. Mater.* **2018**, *47*, 910.
[43] A. Azizi, S. Eichfeld, G. Geschwind, K. Zhang, B. Jiang, D. Mukherjee, L. Hossain, A. F. Piasecki, B. Kabius, J. A. Robinson, N. Alem, *ACS Nano* **2015**, *9*, 4882.
[44] S. M. Eichfeld, L. Hossain, Y. C. Lin, A. F. Piasecki, B. Kupp, A. G. Birdwell, R. A. Burke, N. Lu, X. Peng, J. Li, A. Azcatl, S. McDonnell, R. M. Wallace, M. J. Kim, T. S. Mayer, J. M. Redwing, J. A. Robinson, *ACS Nano* **2015**, *9*, 2080.
[45] D. Dumcenco, D. Ovchinnikov, K. Marinov, P. Lazić, M. Gibertini, N. Marzari, O. L. Sanchez, Y. C. Kung, D. Krasnozhon, M. W. Chen, S. Bertolazzi, P. Gillet, A. Fontcuberta I Morral, A. Radenovic, A. Kis, *ACS Nano* **2015**, *9*, 4611.
[46] Z. Zhang, Y. Gong, X. Zou, P. Liu, P. Yang, J. Shi, L. Zhao, Q. Zhang, L. Gu, Y. Zhang, *ACS Nano* **2019**, *13*, 885.
[47] K. Suenaga, H. G. Ji, Y. C. Lin, T. Vincent, M. Maruyama, A. S. Aji, Y. Shiratsuchi, D. Ding, K. Kawahara, S. Okada, V. Panchal, O. Kazakova, H. Hibino, K. Suenaga, H. Ago, *ACS Nano* **2018**, *12*, 10032.
[48] C. Kastl, C. T. Chen, R. J. Koch, B. Schuler, T. R. Kuykendall, A. Bostwick, C. Jozwiak, T. Seyller, E. Rotenberg, A. Weber-Bargioni, S. Aloni, A. M. Schwartzberg, *2D Mater.* **2018**, *5*, 045010.
[49] Y. C. Lin, C. Y. S. Chang, R. K. Ghosh, J. Li, H. Zhu, R. Addou, B. Diaconescu, T. Ohta, X. Peng, N. Lu, M. J. Kim, J. T. Robinson, R. M. Wallace, T. S. Mayer, S. Datta, L. J. Li, J. A. Robinson, *Nano Lett.* **2014**, *14*, 6936.
[50] M. Okada, T. Sawazaki, K. Watanabe, T. Taniguch, H. Hibino, H. Shinohara, R. Kitaura, *ACS Nano* **2014**, *8*, 8273.
[51] S. Wang, X. Wang, J. H. Warner, *ACS Nano* **2015**, *9*, 5246.
[52] A. Yan, J. Velasco, S. Kahn, K. Watanabe, T. Taniguchi, F. Wang, M. F. Crommie, A. Zettl, *Nano Lett.* **2015**, *15*, 6324.
[53] P. Gehring, B. F. Gao, M. Burghard, K. Kern, *Nano Lett.* **2012**, *12*, 5137.
[54] D. Fu, X. Zhao, Y. Y. Zhang, L. Li, H. Xu, A. R. Jang, S. I. Yoon, P. Song, S. M. Poh, T. Ren, Z. Ding, W. Fu, T. J. Shin, H. S. Shin, S. T. Pantelides, W. Zhou, K. P. Loh, *J. Am. Chem. Soc.* **2017**, *139*, 9392.
[55] J. Kampmeier, S. Borisova, L. Plucinski, M. Luysberg, G. Mussler, D. Grützmacher, *Cryst. Growth Des.* **2015**, *15*, 390.
[56] F. Bonell, M. G. Cuxart, K. Song, R. Robles, P. Ordejón, S. Roche, A. Mugarza, S. O. Valenzuela, *Cryst. Growth Des.* **2017**, *17*, 4655.
[57] I. Levy, T. A. Garcia, S. Shafique, M. C. Tamargo, *J. Vac. Sci. Technol., B: Nanotechnol. Microelectron.: Mater., Process., Meas., Phenom.* **2018**, *36*, 02D107.
[58] X. Zhang, F. Zhang, Y. Wang, D. S. Schulman, T. Zhang, A. Bansal, N. Alem, S. Das, V. H. Crespi, M. Terrones, J. M. Redwing, *ACS Nano* **2019**, *13*, 3341.
[59] N. V. Tarakina, S. Schreyeck, M. Luysberg, S. Grauer, C. Schumacher, G. Karczewski, K. Brunner, C. Gould, H. Buhmann, R. E. Dunin-Borkowski, L. W. Molenkamp, *Adv. Mater. Interfaces* **2014**, *1*, 1400134.

[60] L. Chen, B. Liu, M. Ge, Y. Ma, A. N. Abbas, C. Zhou, *ACS Nano* **2015**, *9*, 8368.
[61] S. El Kazzi, W. Mortelmans, T. Nuytten, J. Meersschaut, P. Carolan, L. Landeloos, T. Conard, I. Radu, M. Heyns, C. Merckling, *J. Appl. Phys.* **2018**, *123*, 135702.
[62] S. H. Sung, N. Schnitzer, L. Brown, J. Park, R. Hovden, *Phys. Rev. Mater.* **2019**, *3*, 064003.
[63] H. P. Komsa, A. V. Krasheninnikov, *Adv. Electron. Mater.* **2017**, *3*, 1600468.
[64] T. H. Ly, D. J. Perello, J. Zhao, Q. Deng, H. Kim, G. H. Han, S. H. Chae, H. Y. Jeong, Y. H. Lee, *Nat. Commun.* **2016**, *7*, 10426.
[65] Z. Y. Wang, H. D. Li, X. Guo, W. K. Ho, M. H. Xie, *J. Cryst. Growth* **2011**, *334*, 96.
[66] A. Rajan, K. Underwood, F. Mazzola, P. D. C. King, *Phys. Rev. Mater.* **2020**, *4*, 14003.
[67] T. Björkman, A. Gulans, A. V. Krasheninnikov, R. M. Nieminen, *Phys. Rev. Lett.* **2012**, *108*, 235502.

